

Platform for designing bipartite entangled quantum frequency combs based on silicon nitride microring resonators

Nianqin Li, Bo Ji, Yang Shen, and Guangqiang He^{iD*}

State Key Laboratory of Advanced Optical Communication Systems and Networks, Department of Electronic Engineering, Shanghai Jiao Tong University, Shanghai 200240, China



(Received 21 December 2023; revised 18 April 2024; accepted 3 May 2024; published 29 May 2024)

Integrated Kerr quantum frequency combs (QFCs), with the potential to generate multiple and scalable quantum states, have emerged as a compact, stable, and fundamental resource for broadband entanglement. Here, we build a platform for designing bipartite entangled QFCs via an on-chip silicon nitride microring resonator. By establishing the system quantum dynamics of Kerr nonlinear microresonators, our platform can support up to 12 continuous-variable quantum modes, in the form of six simultaneously two-mode squeezed pairs under the influence of hysteresis. The entanglement degree of frequency-mode pairs is dependent on the resonator structure and ambient temperature. By adjusting the cavity temperature, we can optimize the performance of entanglement under certain injected pump power and pump detuning. Our comprehensive QFC designing process and entanglement distribution control may ameliorate the generation and optimization of entanglement.

DOI: [10.1103/PhysRevApplied.21.054058](https://doi.org/10.1103/PhysRevApplied.21.054058)

I. INTRODUCTION

Optical quantum states with multimode entanglement among the quantum frequency comb (QFC) are at the heart of quantum information science. Integrated Kerr optical frequency combs have revolutionized our fundamental understanding of quantum mechanics, with direct applications for quantum communication and computation [1,2]. Once a Kerr resonator is weakly pumped, resonator modes below the optical parametric oscillation (OPO) threshold are populated in pairs through spontaneous parametric processes. In this quantum realm, Kerr QFCs allow for applications consisting of time-bin entangled circuits [3], photon-pair sources [4,5], quadrature-squeezed vacuum states [6], heralded single-photon [7] and multiuser quantum networks [8].

Although the generation of QFCs started with discrete bulky optical devices, the advancements in integrated photonics have significantly broadened the potential applications of Kerr quantum frequency combs. On-chip QFCs surpass the limitations of traditional free-space optical parametric oscillators (OPOs) in terms of maneuverability, integration, and scalability. Also, the structural features of integrated microresonators exhibit strong mode confinement, which leads to high nonlinearity. Recent research has honed in on the high degree of squeezing [9] and the underlying quantum processes of soliton microcombs [10] within nanophotonic devices.

Silicon nitride, compatible with CMOS technology, possesses exceptional properties such as low loss and a wide transparent window. The properties of optical frequency combs generated in Si_3N_4 microresonators hinge on the waveguide dispersion of the cavity. Thus, waveguide dispersion engineering is crucial in shaping classic frequency combs [11]. Although the implementation of structural modeling and simulation based on silicon nitride microresonators have been rarely emphasized in the quantum realm so far, advanced CMOS technology enables the fine design of ring-bus coupling rate and dispersion of the microresonators through cavity structure engineering. Additionally, the thermoelectric heater can be firmly attached to the microresonator during the CMOS process. Thus, each mode of the QFC can be fine tuned by modifying the microresonator structure and adjusting the ambient temperature. By introducing the bipartite-entanglement criterion, we can measure the degree of entanglement, thus providing a quantitative measurement of the impact of structure and temperature on entanglement performance.

In our work, we develop a comprehensive platform that enables dispersion and coupling engineering for integrated silicon nitride microring resonators. Our platform implements the OPO theory to establish the quantum dynamics of third-order nonlinear microresonators, including self-phase modulation (SPM), cross-phase modulation (XPM), and four-wave mixing (FWM). Also, our platform allows for the extraction of resonator structure parameters and supports thermal adjustment. Through modifications to the microresonator, we successfully generate bipartite entangled frequency combs with up to 12 channels

*Corresponding author: gqhe@sjtu.edu.cn

(six pairs), ideal for multichannel quantum information networks. These QFCs exhibit temperature-dependent properties, making them versatile and flexible resources for quantum entanglement. Furthermore, we can depict the panorama of entanglement distribution in each mode according to the bipartite entanglement criterion, so that the performance of entanglement under certain initially set injected pump power and pump detuning can be optimized by adjusting the ambient temperature of the cavity. The simulation of entanglement distribution control may provide another avenue for the field of QFC design. By combining our silicon nitride microresonator with a tunable laser integrated on the same material [12], it is possible to generate an entirely on-chip entanglement resource. This advancement holds the potential to broaden the utilization of fully integrated entanglement resources in the field of quantum information process and quantum teleportation.

This paper is structured in the following manner. Section II outlines the simulation model for an integrated silicon nitride microresonator and introduces dispersion and coupling engineering. Section III presents a theoretical model for four-wave mixing in a microresonator based on the OPO theory and establishes quantum entanglement criteria for signal and idler. In Sec. IV, the necessary variables for the simulation process are extracted and implemented, while also examining the effects of these variables and temperature on the degree of entanglement. Finally, Sec. V provides a summary of the results, showcasing the development of a platform for designing bipartite entangled quantum frequency combs based on silicon nitride microring resonators.

II. SIMULATION MODEL OF MICRORING RESONATORS

Figure 1 illustrates the third-order nonlinear process involved in the generation of Kerr optical frequency combs. Due to the third-order nonlinearity, the input continuous-wave pump light (Ω_p) undergoes the four-wave mixing effect, leading to the generation of signal (Ω_s) and idler (Ω_i) light with the energy of different state modes redistributed. Figure 2(a) illustrates a typical structure of a microring resonator with an add-through coupling configuration, to which the OPO theory is applicable. The structure of our on-chip microring resonator consists of one bus waveguide and one ring waveguide, where the silicon nitride rib waveguides are buried into the SiO_2 cladding. The cladding serves as a protection layer and enables the placement of an integrated microheater, which is tightly attached to the resonator. With the assistance of the microheater, resonance tuning and stabilization become tractable [13,14]. Without loss of generality, the side view of the resonator structure is illustrated in Fig. 2(b). The gap is defined as the shortest straight-line distance at the half height ($h/2$) of the two waveguides. Since the light field

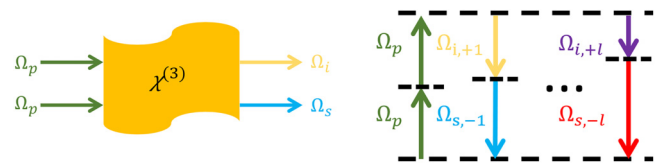


FIG. 1. A schematic depiction of the third-order nonlinear process in the generation of Kerr optical frequency combs.

propagates along the x axis in Fig. 2(a), A_{eff} denotes the effective cross-section area of the ring waveguide [15].

$$A_{\text{eff}} = \frac{\left(\int \int_{-\infty}^{+\infty} |F(y, z)|^2 dy dz \right)^2}{\int \int_{-\infty}^{+\infty} |F(y, z)|^4 dy dz}, \quad (1)$$

where $F(y, z)$ is the mode distribution in Si_3N_4 and SiO_2 , and we assume that the mode distribution in the resonator is time invariant.

The geometry of the coupling region is directly related to the ring-bus coupling rate, making it easy to extract the

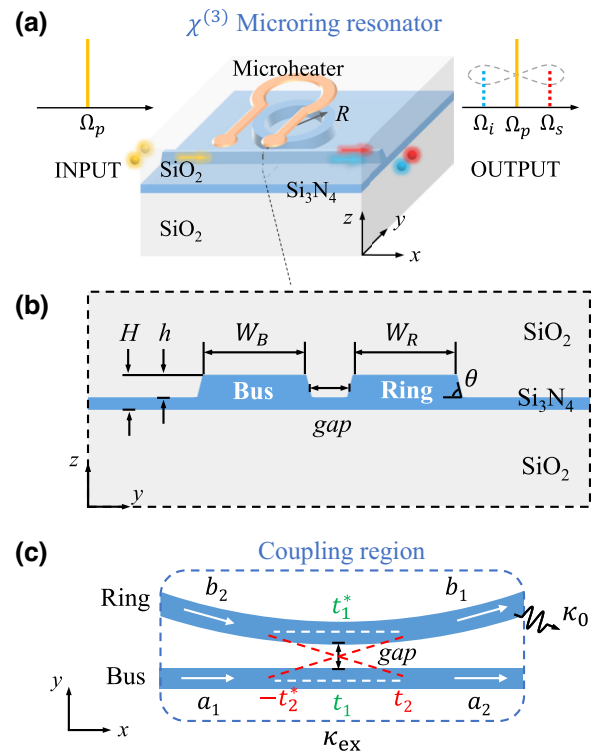


FIG. 2. On-chip add-through microring resonator. (a) Three-dimensional scheme of the resonator. R is the mean radius of the ring waveguide. (b) Profile of rib waveguides. θ is the tilt angle of the sidewall. The gap is defined at $h/2$. (c) Enlarged view of the coupling region and its input-output schematic. κ_0 , loss coupling rate; κ_{ex} , ring-bus coupling rate. Constants t_1 and t_2 satisfy $|t_1|^2 + |t_2|^2 = 1$. Note that bus waveguides are not limited to being straight.

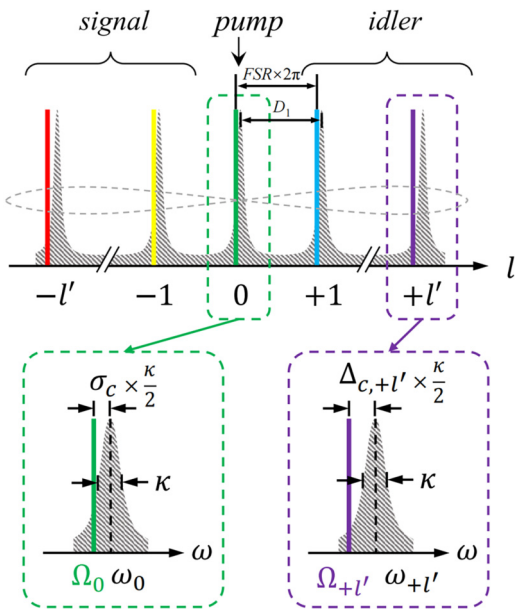


FIG. 3. Resonances under anomalous dispersion. Solid lines are perfectly equispaced, which represents the location of the output comb lines. Gray slashes represent the location of the resonances under anomalous dispersion. In the case of mode 0, the enlarged subgraph illustrates the relationship between the laser frequency Ω_0 (i.e., Ω_p), cold-resonance frequency ω_0 , loaded linewidth κ , and the normalized cold cavity pump detuning (red detuned) $\sigma_c = (2/\kappa)(\omega_0 - \Omega_0)$. As for mode $+l'$, the normalized cold cavity detuning $\Delta_{c,+l'} = (2/\kappa)(\omega_{+l'} - \Omega_{+l'})$. Assume the considered modes share the same κ .

coupling rate, which indicates the input-output relationship of the resonator [16].

We solely consider the fundamental *TE* mode, leading to a Lorentzian shape envelope of cavity resonance (depicted in Fig. 3, shaded area). Due to the frequency dependence of material refractive index $n(\omega)$, resonances are not equispaced in the spectrum. To adjust cavity variables including detuning, dispersion, intracavity temperature, coupling, and loss rate through our designing platform, theoretical preparation is necessary.

A. Detuning, dispersion, and intracavity temperature

In this section, the properties of detuning and dispersion versus intracavity temperature are discussed. The relative mode number l ($l \in \mathbb{Z}$) is introduced to define the state modes alongside the pump mode ω_0 ($l = 0$). Apply the Taylor expansion for the resonance modes around ω_0 [1]:

$$\omega_l = \omega_0 + D_1 l + \frac{D_2}{2} l^2 + \dots = \omega_0 + \sum_{n=1}^{\infty} D_n \frac{l^n}{n!}, \quad (2)$$

where $D_n = d^n \omega_l / dl^n$ at $l = 0$. In particular, $v_f = D_1 / 2\pi$, which is defined as the free spectral range (FSR) of the frequency comb. D_2 is related to the group velocity dispersion

(GVD), and $D_2 > 0$ ($D_2 < 0$) indicates anomalous (normal) dispersion. When $n \geq 3$, we assume $D_n = 0$ so as to define the integrated dispersion $D_{\text{int}} = \omega_l - \omega_0 - D_1 l$ [17], which can be well approximated by a quadratic polynomial around ω_0 . The case of anomalous dispersion in silicon nitride microring resonators is concerned, which has been well established in the generation of bright optical frequency combs [18].

We assume that the cavity holds the same temperature throughout the microring structure at any given moment. Resonance modes at temperature T with thermally induced frequency shift is

$$\omega_l(T) = \omega_l(T_0) \left[1 - \left(\frac{\alpha_n}{n_0} + \alpha_L \right) T_\delta \right], \quad (3)$$

where $T_\delta = T - T_0$, the holistic temperature difference from the reference temperature. $T_0 = 20^\circ\text{C}$, the reference temperature of the microresonator. $\alpha_n = dn/dT = 2.45 \times 10^{-5}/^\circ\text{C}$ and $\alpha_L = dL/(dT) = 3.30 \times 10^{-6}/^\circ\text{C}$, the thermo-optic coefficient and the thermal expansion coefficient of Si_3N_4 , respectively [19,20]. $n_0 = 1.996$, the refractive index of Si_3N_4 around ω_0 .

Assume that the pump power is zero (the frequency shift caused by pump power through nonlinearity effect can be ignored) and only focus on the thermally induced frequency shift of the resonance modes. The pump detuning at temperature T is

$$\sigma_c = \omega_0(T) - \Omega_0(T). \quad (4)$$

Irrelevant to temperature T , the comb lines of QFCs are always equispaced, which has nothing to do with D_{int} :

$$\Omega_l(T) = \Omega_0(T) + D_1 l. \quad (5)$$

While the resonance modes at ambient temperature T_0 is

$$\omega_l(T_0) = \omega_0(T_0) + D_1 l + \frac{D_2}{2} l^2. \quad (6)$$

Consider Eq. (2)–(5), the normalized cold-cavity detuning Δ_c at mode l can be scaled to the cavity resonance half-width $\kappa/2$:

$$\begin{aligned} \Delta_{c,l} &= \frac{2}{\kappa} (\omega_l(T) - \Omega_l(T)) \\ &= \sigma_c + \frac{D_2}{\kappa} l^2 - \Delta_T, \end{aligned} \quad (7)$$

where $\Delta_T = 2/\kappa(D_1 l + (D_2/2)l^2)[(\alpha_n/n_0) + \alpha_L]T_\delta$ and $\sigma_c = 2/\kappa(\omega_0 - \Omega_0)$, the normalized cold cavity pump detuning. Thus, the relationship between detuning, dispersion, and intracavity temperature is developed.

B. Coupling, loss, and gap

In this section, we discuss the relationship between the input-output parameters, namely the coupling (γ) and loss rate (μ) of the cavity, and the autologous cavity parameters: gap, κ and quality factors. We assume that the loss of the resonator is modeled as an effective phantom channel [21,22], and the beam-splitter transmission feature [23] can be applied to ensure that $\gamma \ll 1$ and $\mu \ll 1$. As shown in Fig. 2(c), we set $b_2 = 0$ and simulate the transmission $|t_1|^2$. Therefore, $\gamma = |t_2|^2/2 = (1 - |t_1|^2)/2$ and μ is simplified as $\mu = \alpha L/2$ [24], where $L = 2\pi R$. Besides, $\alpha \approx f_0/(Q_0 \times R \times v_f)$ is the absorption coefficient (m^{-1}) [25], where f_0 (Hz) is the resonance frequency.

Next, we set $b_2 = 0$ and scan the transmission ($|t_1|^2$) from the add port to the through port as the gap varies. The ratio $r = \gamma/\mu$ represents the relationship between coupling and internal loss. When $r < 1$, it indicates undercoupling, $r > 1$ represents overcoupling, and $r = 1$ represents critical coupling.

Since the intrinsic quality factor (Q_0) is closely related to the manufacturing process of the resonator, Q_0 should be properly set in the simulation based on state-of-the-art silicon nitride microring resonators [26,27]. Meanwhile, the value of the loss coupling rate (rad/s) $\kappa_0 = \omega_0/Q_0 \approx c\alpha/n_g = 2v_f \times \mu$, where $n_g = 2.0396$ is the group refractive index of silicon nitride around Ω_0 . The total loss rate $\kappa = \kappa_0(1 + r) = 2v_f \times \Gamma$ [16] and the ring-bus coupling rate $\kappa_{\text{ex}} = \kappa - \kappa_0 = \omega_0/Q_{\text{ex}} = 2v_f \times \gamma$, where Q_{ex} is the external quality factor. And the total quality factor Q satisfies

$$\frac{1}{Q} = \frac{1}{Q_0} + \frac{1}{Q_{\text{ex}}}. \quad (8)$$

Therefore, we can link the gap with Q_{ex} using the ratio r .

In addition, the experimental method for extracting quality factors is introduced in Ref. [28].

C. Actual simulation

We aim to design a dispersion-flat waveguide in the communication band to minimize the phase mismatch of FWM processes [Eq. (9)]. In order to generate more maneuverable entanglement state pairs, dispersion engineering is crucial to ensure optimal energy conservation and phase-matching conditions by fitting D_{int} to zero in the widest possible spectral range.

$$\Delta k = \frac{2\omega_p n(\omega_p)}{c} - \frac{\omega_s n(\omega_s)}{c} - \frac{\omega_i n(\omega_i)}{c} = 0. \quad (9)$$

We choose a typical microring structure with anomalous dispersion that can generate classical optical soliton [26]. According to Fig. 2, we design $R = 23 \mu\text{m}$, $W_R = W_B =$

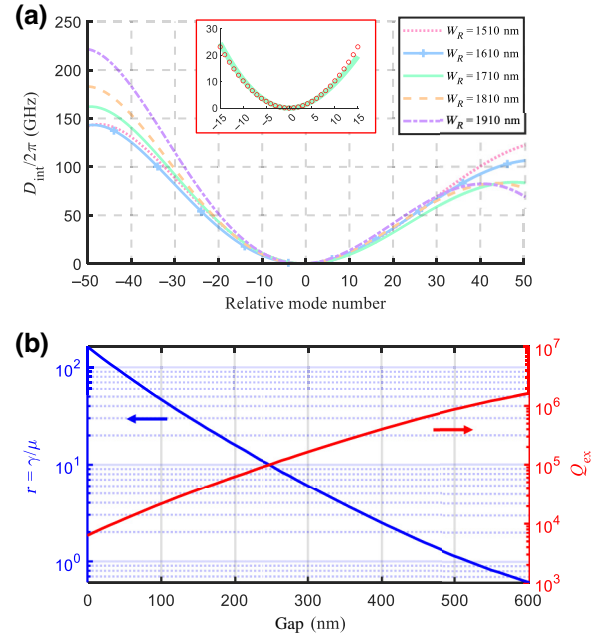


FIG. 4. (a) Dispersion simulation with fifth-order polynomial fit. Simulated dispersion D_{int} for oxide-coated 23- μm -radius Si_3N_4 rings with varied waveguide width W_R . The inserted graph shows the good fit of D_{int} to the quadratic function around ω_0 . Note that the frequency of mode 0 is different at varied W_R . (b) Coupling simulation. Simulated $r = \gamma/\mu$ and Q_{ex} for oxide-coated 23- μm -radius Si_3N_4 rings with varied gap. The bus waveguide width $W_B = 1710 \text{ nm}$. For both (a),(b), the waveguide height $H = h = 780 \text{ nm}$. Material dispersion comes from Ref. [29].

1710 nm, $H = h = 780 \text{ nm}$, $\theta = 90^\circ$. Only the fundamental TE mode is taken into consideration. The temperature in the dispersion simulation is T_0 .

Figure 4 shows dispersion and coupling simulation results. $v_f = 973.766 \text{ GHz}$. Frequency of mode 0: $f_0 = 192.669 \text{ THz}$. $D_2 = 2.0583 \times 2\pi \times 10^8 \text{ rad/s}$. $A_{\text{eff}} = 1.1157 \mu\text{m}^2$. We assume the intrinsic quality factor $Q_0 = 10^6$, thus $\mu = 1.21 \times 10^9$. Set $r = \gamma/\mu = 1.222$ (overcoupling), thus gap = 490 nm. The threshold power $P_{\text{th}} = 11.2 \text{ mW}$.

III. SYSTEM DYNAMICS

In this section, we will expound the quantum dynamics in the resonator based on Sec. II.

A. Hamiltonian

System hamiltonian can describe the optical nonlinear process in the realm of quantum mechanics. In our work, we concentrate on the pump-degenerate FWM, where the pump mode frequency is $\omega_p = \omega_0$ and signal (idler) is generated at $\omega_s = \omega_{-l}$ ($\omega_i = \omega_{+l}$), $l > 0$. Each resonance mode is described by an annihilation operator \hat{a}_j , $j = p, s, i$. The total hamiltonian of the system consists of two

parts, one is the free Hamiltonian \hat{H}_0 of the three modes, and the other is the nonlinear interaction Hamiltonian \hat{H}_{NL} . The free Hamiltonian \hat{H}_0 is given by

$$\hat{H}_0 = \hbar \sum_{j=p,s,i} \omega_j \hat{a}_j^\dagger \hat{a}_j. \quad (10)$$

The nonlinear interaction Hamiltonian \hat{H}_{NL} is given by Eq. (11), which can describe the interaction between the pump and a particular pair of signal and idler:

$$\begin{aligned} \hat{H}_{\text{NL}} = & -\hbar g \left[\frac{1}{2} \left(\hat{a}_p^\dagger \hat{a}_p^\dagger \hat{a}_p \hat{a}_p + \hat{a}_s^\dagger \hat{a}_s^\dagger \hat{a}_s \hat{a}_s + \hat{a}_i^\dagger \hat{a}_i^\dagger \hat{a}_i \hat{a}_i \right) \right. \\ & + 2 \left(\hat{a}_p^\dagger \hat{a}_s^\dagger \hat{a}_p \hat{a}_s + \hat{a}_p^\dagger \hat{a}_i^\dagger \hat{a}_p \hat{a}_i + \hat{a}_s^\dagger \hat{a}_i^\dagger \hat{a}_s \hat{a}_i \right) \\ & \left. + \left(\hat{a}_s^\dagger \hat{a}_i^\dagger \hat{a}_p \hat{a}_p + \hat{a}_p^\dagger \hat{a}_p^\dagger \hat{a}_s \hat{a}_i \right) \right]. \end{aligned} \quad (11)$$

The first bracket represents the self-phase modulation (SPM), the second bracket represents the cross-phase modulation (XPM), and the last bracket represents the four-wave mixing (FWM). The SPM and XPM terms are responsible for the intensity-dependent frequency shift of the resonance, and they play an indispensable role in the entanglement properties of the system. The FWM term represents the energy redistribution we expect. Here, the lower bound estimate of nonlinear coupling coefficient $g = \hbar \omega_0^2 c n_2 / (n_0^2 V_{\text{eff}})$ [30], representing the per photon frequency shift of the resonance due to the $\chi^{(3)}$ nonlinearity. \hbar , Planck's constant over 2π . c , the vacuum speed of light. n_2 , the nonlinear index of Si_3N_4 , which is associated with the refractive index n_0 . In our Si_3N_4 microresonator, $n_2 = 2.6 \times 10^{-19} \text{ m}^2/\text{W}$ [31]. V_{eff} , the effective mode volume, which can be defined by [32]

$$V_{\text{eff}} = \frac{\int n_0^2 |F(x, y, z)|^2 dV \int |F(x, y, z)|^2 dV}{\int n_0^2 |F(x, y, z)|^4 dV}. \quad (12)$$

When the WGM resonator is a microring resonator, the higher bound estimate of V_{eff} can be approximated by

$V_{\text{eff}} \approx A_{\text{eff}} \times 2\pi R$ [30]. $R = (D_{\text{in}} + D_{\text{ou}})/4$, the radius of microring resonator, where D_{in} refers to the inner diameter of microring resonator, and D_{ou} refers to the outer diameter of microring resonator.

Hence, the total Hamiltonian is given by

$$\hat{H} = \hat{H}_0 + \hat{H}_{\text{NL}}. \quad (13)$$

B. Heisenberg-Langevin equations

We apply the Heisenberg-Langevin equation [33] to analyze the evolution process of the three modes:

$$\dot{\hat{a}}_j = -\frac{i}{\hbar} [\hat{a}_j, \hat{H}] + V, \quad j = p, s, i \quad (14a)$$

$$V = -\Gamma \sum_j \hat{a}_j + \sqrt{2\gamma} \sum_j \hat{a}_j^{\text{in}} + \sqrt{2\mu} \sum_j \hat{a}_j^{\text{loss}}, \quad (14b)$$

where $\Gamma = \gamma + \mu = \kappa/(2\nu_f)$, $\gamma = \kappa_{\text{ex}}/(2\nu_f)$, and $\mu = \kappa_0/(2\nu_f)$. According to Sec. 2, we assume that the considered modes have similar field profiles, and they share the same total loss rate κ , loss coupling rate κ_0 , and ring-bus coupling rate κ_{ex} , in which $\kappa = \kappa_0 + \kappa_{\text{ex}}$. Annihilation operators \hat{a}^{in} and \hat{a}^{loss} are the incoming and loss modes of the resonator, which satisfies

$$\begin{cases} \langle \hat{a}_j^{\text{loss}}(t) \rangle = \langle \hat{a}_s^{\text{in}}(t) \rangle = \langle \hat{a}_i^{\text{in}}(t) \rangle = 0, \\ \langle \hat{a}_p^{\text{in}}(t) \rangle = A^{\text{in}} = \sqrt{\frac{P_{\text{in}}}{\hbar \Omega_0}}, \\ \langle \hat{a}_j^{\text{loss}}(t) \hat{a}_j^{\dagger, \text{loss}}(t') \rangle = \langle \hat{a}_j^{\text{in}}(t) \hat{a}_j^{\dagger, \text{in}}(t') \rangle = \delta(t - t'), \end{cases} \quad (15)$$

where P_{in} (watts) is the pump laser power in the bus waveguide.

We replace \hat{a}_j with $\hat{a}_j e^{-i\Omega_j t}$ so as to apply the rotating-wave approximation (RWA). Ω_j are frequencies that perfectly fulfill the energy conservation with $2\Omega_p = \Omega_s + \Omega_i$ (i.e., $2\Omega_0 = \Omega_{-l} + \Omega_{+l}$).

Finally, the Heisenberg-Langevin equations for the pump, signal, and idler modes satisfy

$$\begin{cases} \frac{d\hat{a}_p}{dt} = ig \left[\left(\hat{a}_p^\dagger \hat{a}_p + 2\hat{a}_s^\dagger \hat{a}_s + 2\hat{a}_i^\dagger \hat{a}_i \right) \hat{a}_p + 2\hat{a}_p^\dagger \hat{a}_s \hat{a}_i \right] - \Gamma \hat{a}_p - i\frac{\kappa}{2} \sigma_c \hat{a}_p + \sqrt{2\gamma} \hat{a}_p^{\text{in}} + \sqrt{2\mu} \hat{a}_p^{\text{loss}}, \\ \frac{d\hat{a}_s}{dt} = ig \left[\left(2\hat{a}_p^\dagger \hat{a}_p + \hat{a}_s^\dagger \hat{a}_s + 2\hat{a}_i^\dagger \hat{a}_i \right) \hat{a}_s + \hat{a}_p^2 \hat{a}_i^\dagger \right] - \Gamma \hat{a}_s - i\frac{\kappa}{2} \Delta_{-l} \hat{a}_s + \sqrt{2\gamma} \hat{a}_s^{\text{in}} + \sqrt{2\mu} \hat{a}_s^{\text{loss}}, \\ \frac{d\hat{a}_i}{dt} = ig \left[\left(2\hat{a}_p^\dagger \hat{a}_p + 2\hat{a}_s^\dagger \hat{a}_s + \hat{a}_i^\dagger \hat{a}_i \right) \hat{a}_i + \hat{a}_p^2 \hat{a}_s^\dagger \right] - \Gamma \hat{a}_i - i\frac{\kappa}{2} \Delta_{+l} \hat{a}_i + \sqrt{2\gamma} \hat{a}_i^{\text{in}} + \sqrt{2\mu} \hat{a}_i^{\text{loss}}. \end{cases} \quad (16)$$

Since the SPM and XPM process have been taken into consideration through the nonlinear interaction Hamiltonian \hat{H}_{NL} , in Eq. (16), σ_c is the normalized cold

cavity pump detuning, Δ_{-l} and Δ_{+l} are the normalized cold cavity detuning for signal mode and idler mode, respectively.

C. Steady-state equations

The temporal evolution of cavity modes is described by Eq. (16). To obtain the solutions of Eq. (16), we apply the linearization approach by expanding each field operator \hat{a}_j as a sum of its steady-state mean value α_j and fluctuation operator $\delta\hat{a}_j$, i.e., $\hat{a}_j = \alpha_j + \delta\hat{a}_j$. In steady state, α_j does not evolve, so by setting $\delta\hat{a}_j = 0$ and $d\alpha_j/dt = 0$, Heisenberg-Langevin equations can be formed to steady state. Also, under this circumstance the input of the signal

and idler, the loss of the signal, idler, and pump are all in vacuum state, so $\alpha_s^{\text{in}} = \alpha_i^{\text{in}} = \alpha_p^{\text{loss}} = 0$.

Without loss of generality, we consider the phase of the external pump as a reference. Thus we set $\alpha_j = A_j e^{i\theta_j}$, $\alpha_p^{\text{in}} = A^{\text{in}} e^{i\theta_{\text{in}}}$, $\phi = \theta_s + \theta_i - 2\theta_p$, $\psi = \theta_{\text{in}} - \theta_p$. For simplicity, we set $A_s = A_i = A$ and $\Delta_{+l} = \Delta_{-l} = \Delta$, with the scale to the cavity resonance half-width $\kappa/2$ omitted. Define the external pump power $F = \sqrt{(2\gamma g/\hbar\Omega_0\Gamma^3)P_{\text{in}}}$ [34], $A^{\text{in}} = F\sqrt{\Gamma^3/2\gamma g}$. Based on these variables, we get

$$\begin{cases} \Gamma^2 A^4 + [\Delta A^2 - gA^2(2A_p^2 + 3A^2)]^2 = g^2 A_p^4 A^4, \\ 2\gamma A_p^2 (A^{\text{in}})^2 = (\Gamma A_p^2 + 2\Gamma A^2)^2 + [\sigma_c A_p^2 - gA_p^2(A_p^2 + 4A^2) - 2\Delta A^2 + 2g(2A_p^2 + 3A^2)A^2]^2, \end{cases} \quad (17)$$

Eq. (17) contains five variables: A_p , A , A^{in} , σ_c , and Δ . By giving an actual value to any two of them, we can tell the relationship between the remaining three variables numerically, which means any two of the remaining three variables can be represented by a function of the other one variable.

D. Quantum fluctuation equations

In order to uncover the quantum properties of the signal and idler, the quantum fluctuation equations of Eq. (16) are required. Since we have calculated the steady-state equations, we can modify Eq. (16) by setting $\hat{a}_j = \delta\hat{a}_j$. We treat the pump field as a classical beam, thus $\delta\hat{a}_p = 0$. Also, high-order fluctuations are neglected.

Define a vector containing the fluctuations of the signal and idler as

$$\delta\hat{\mathbf{A}} = \left(\delta\hat{a}_s e^{-i\theta_s}, \delta\hat{a}_s^\dagger e^{i\theta_s}, \delta\hat{a}_i e^{-i\theta_i}, \delta\hat{a}_i^\dagger e^{i\theta_i} \right)^T, \quad (18)$$

where θ_j is the phase of the mean value $\alpha_j = A_j e^{i\theta_j}$. The time evolution of these fluctuations are given by

$$\frac{1}{\Gamma} \cdot \frac{d\delta\hat{\mathbf{A}}}{dt} = M_a \cdot \delta\hat{\mathbf{A}} + T_a^{\text{in}} \cdot \delta\hat{\mathbf{A}}^{\text{in}} + T_a^{\text{loss}} \cdot \delta\hat{\mathbf{A}}^{\text{loss}}, \quad (19)$$

where $T_a^{\text{in}} = \text{diag}(\sqrt{2\gamma}, \sqrt{2\gamma}, \sqrt{2\gamma}, \sqrt{2\gamma})$, $T_a^{\text{loss}} = \text{diag}(\sqrt{2\mu}, \sqrt{2\mu}, \sqrt{2\mu}, \sqrt{2\mu})$. The matrix M_a is derived from the linearization process and its elements are related to the field's mean values and detunings.

The evolution of these fluctuations in frequency domain can be given by Fourier transform. After introducing the input-output relationship of the resonator [23]

$$\hat{a}^{\text{out}} = -\hat{a}^{\text{in}} + \sqrt{2\gamma}\hat{a}, \quad (20)$$

we obtain

$$\begin{aligned} \delta\hat{\mathbf{A}}^{\text{out}}(\omega) &= -\delta\hat{\mathbf{A}}^{\text{in}} + T_a \delta\hat{\mathbf{A}} \\ &= M^{\text{in}}(\omega) \cdot \delta\hat{\mathbf{A}}^{\text{in}} + M^{\text{loss}}(\omega) \cdot \delta\hat{\mathbf{A}}^{\text{loss}}, \end{aligned} \quad (21)$$

where $T_a = \text{diag}(\sqrt{2\gamma}, \sqrt{2\gamma}, \sqrt{2\gamma}, \sqrt{2\gamma})$,

$$M^{\text{in}}(\omega) = T_a (i\omega I - M_a)^{-1} T_a^{\text{in}} - I, \quad (22)$$

$$M^{\text{loss}}(\omega) = T_a (i\omega I - M_a)^{-1} T_a^{\text{loss}}, \quad (23)$$

and I is the identity matrix.

Therefore, the output spectral noise density matrix is defined by

$$\begin{aligned} S_a(\omega) &= \left\langle \delta\hat{\mathbf{A}}^{\text{out}}(\omega) \delta\hat{\mathbf{A}}^{\text{out}, \text{T}}(-\omega) \right\rangle \\ &= M^{\text{in}}(\omega) \\ &\quad \cdot M_c \cdot M^{\text{in}, \text{T}}(-\omega) + M^{\text{loss}}(\omega) \cdot M_c \cdot M^{\text{loss}, \text{T}}(-\omega), \end{aligned} \quad (24)$$

where the matrix

$$M_c = \begin{pmatrix} 0 & 1 & 0 & 0 \\ 0 & 0 & 0 & 0 \\ 0 & 0 & 0 & 1 \\ 0 & 0 & 0 & 0 \end{pmatrix}.$$

E. Bipartite entanglement criterion

To quantitatively analyze the entanglement between signal and idler, we apply the criterion in Ref. [35] to obtain the entanglement degree C_s . We define the amplitude

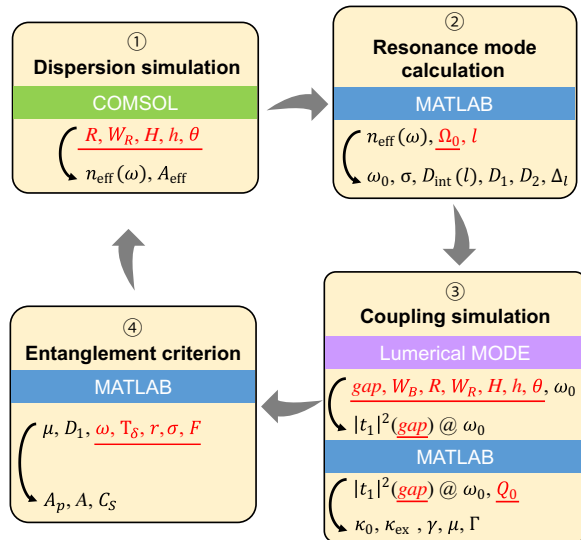


FIG. 5. Simulation flow chart. The red underlined variables may need to be set manually. $|t_1|^2(\text{gap})$ represents the gap-dependent transmission characteristic of the resonator.

$(\hat{x}_j, j = s, i)$ and phase $(\hat{y}_j, j = s, i)$ operators, which are functions of \hat{a}_j and \hat{a}_j^\dagger :

$$\hat{x}_j = \frac{\hat{a}_j + \hat{a}_j^\dagger}{\sqrt{2}}, \quad \hat{y}_j = \frac{-i\hat{a}_j + i\hat{a}_j^\dagger}{\sqrt{2}}. \quad (25)$$

Introduce the sum and subtraction basis:

$$\hat{x}_\pm = \frac{\hat{x}_s \pm \hat{x}_i}{\sqrt{2}}, \quad \hat{y}_\pm = \frac{\hat{y}_s \pm \hat{y}_i}{\sqrt{2}}, \quad (26)$$

and we obtain the fluctuation vector

$$\delta\hat{X}_\pm = (\delta\hat{y}_+, \delta\hat{x}_+, \delta\hat{y}_-, \delta\hat{x}_-)^\top. \quad (27)$$

The spectral noise density matrix $S_{\hat{X}_\pm}(\omega)$ is calculated by

$$S_{\hat{X}_\pm}(\omega) = \langle \delta\hat{X}_\pm(\omega) \delta\hat{X}_\pm^\top(-\omega) \rangle = T_0 \cdot S_a(\omega) \cdot T_0^\top, \quad (28)$$

where the matrix

$$T_0 = \frac{1}{2} \begin{pmatrix} -i & i & -i & i \\ 1 & 1 & 1 & 1 \\ -i & i & i & -i \\ 1 & 1 & -1 & -1 \end{pmatrix}.$$

Since the best attainable squeezing is provided by Schmidt modes [36], we introduce vector $\delta\hat{X}_\pm^{\text{rot}}$ to represent the

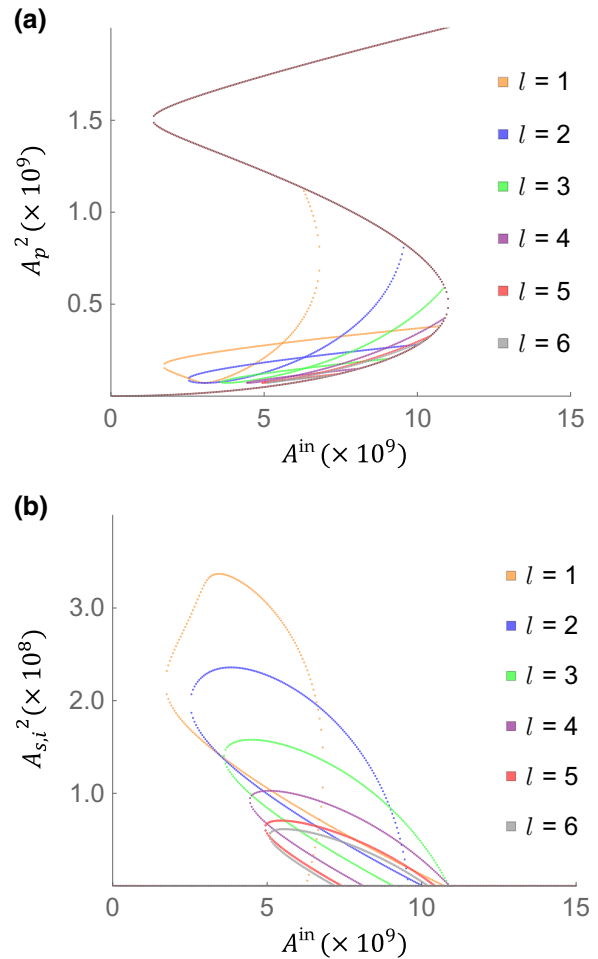


FIG. 6. The intracavity mode amplitude versus injected pump amplitude of our QFC. (a) Pump mode. (b) Signal and idler mode ($T_\delta = 80^\circ\text{C}$, $\sigma_c = 4.5$ GHz).

rotation operation:

$$\delta\hat{X}_\pm^{\text{rot}} = (\delta\hat{y}_+^{\text{rot}}, \delta\hat{x}_+^{\text{rot}}, \delta\hat{y}_-^{\text{rot}}, \delta\hat{x}_-^{\text{rot}})^\top, \quad (29)$$

with $\delta\hat{X}_\pm^{\text{rot}} = M_{\text{rot}} \delta\hat{X}_\pm$. The rotation operation matrix

$$M_{\text{rot}} = \begin{pmatrix} \cos\theta_+ & \sin\theta_+ & 0 & 0 \\ -\sin\theta_+ & \cos\theta_+ & 0 & 0 \\ 0 & 0 & \cos\theta_- & \sin\theta_- \\ 0 & 0 & -\sin\theta_- & \cos\theta_- \end{pmatrix}, \quad (30)$$

where θ_\pm diagonalize the spectral density matrix. And we obtain

$$S_{\hat{X}_\pm}^{\text{rot}}(\omega) = M_{\text{rot}} \cdot S_{\hat{X}_\pm}(\omega) \cdot M_{\text{rot}}^\top. \quad (31)$$

Using above Schmidt modes quadratures, we derive the entanglement criterion [37]:

$$C_s = (\Delta\hat{x}_-^{\text{rot}})^2 + (\Delta\hat{y}_+^{\text{rot}})^2 - |\Theta|, \quad (32)$$

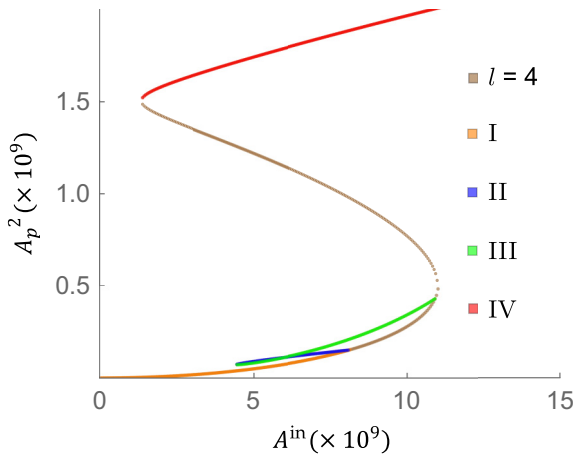


FIG. 7. The intracavity pump-mode amplitude versus injected pump amplitude of the fourth mode ($T_\delta = 80^\circ\text{C}$, $\sigma_c = 4.5\text{ GHz}$).

where $(\Delta\hat{x}_-^{\text{rot}})^2 = S_{\hat{X}_-}^{\text{rot}}(\omega)(4, 4)$, $(\Delta\hat{y}_+^{\text{rot}})^2 = S_{\hat{X}_+}^{\text{rot}}(\omega)(1, 1)$, and $\Theta = \cos(\theta_+ - \theta_-)$. Negative values of C_s imply entanglement between signal and idler.

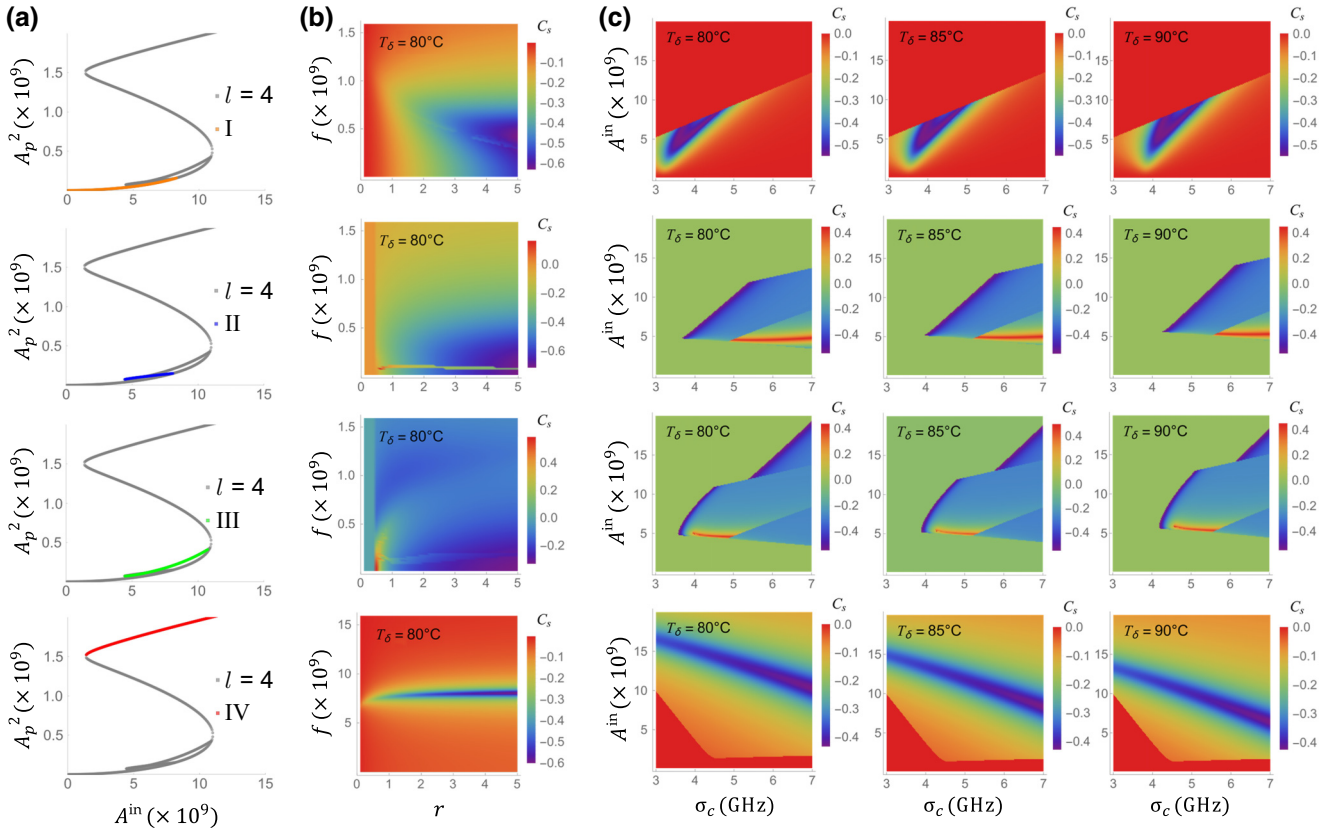


FIG. 8. (a) The four stages of the fourth mode. (b) The entanglement distribution in the regime of coupling rate r and observation frequency f ($\sigma_c = 4.5\text{ GHz}$, $A^{\text{in}} = 6 \times 10^9$). (c) The entanglement distribution in the regime of pump detuning σ_c and injected pump power A^{in} ($r = 1.222$, observation angular frequency $\omega = 10^4$ at stages I, II, and III, and $\omega = 6 \times 10^{10}$ at stage IV).

IV. ENTANGLEMENT ANALYSIS

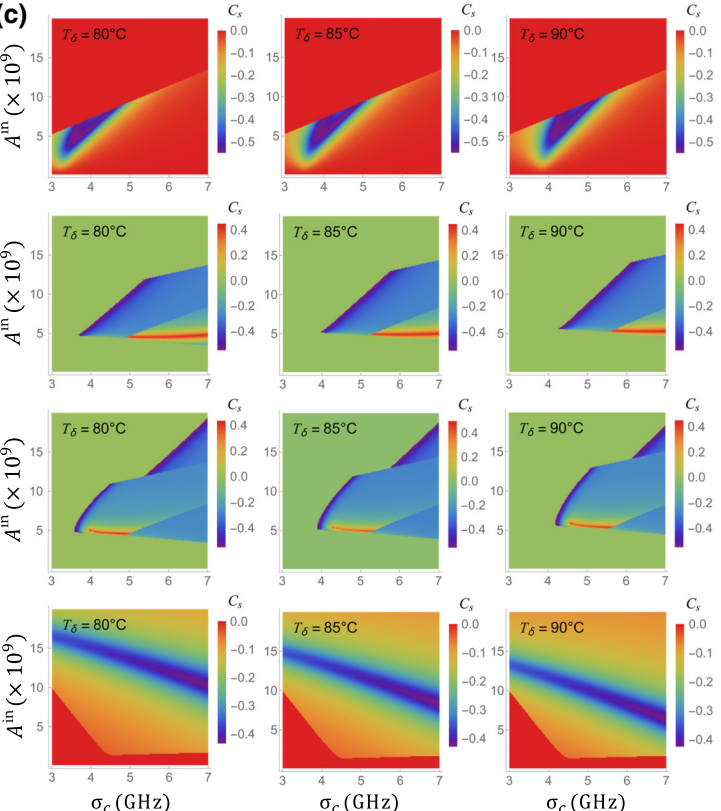
In this section, we will study the signal-idler bipartite entanglement through simulation results with practicable parameters.

A. Simulation process

Our entire simulation process is illustrated in Fig. 5. First, the structural parameters of the microring resonator need to be provided to simulate the effective refractive index $n_{\text{eff}}(\omega)$. Second, we determine the center frequency of the pump light ($\Omega_0 \approx 193\text{ THz} \times 2\pi$) and calculate the resonance mode and D_{int} . Next, we simulate the coupling relationship between the microring resonator and the bus waveguide, which allows us to extract parameters such as κ_{ex} . Finally, we evaluate the entanglement relationship between the signal and idler by using the criterion of $C_s < 0$ as a signature of bipartite entanglement.

B. Bipartite entangled QFCs

By examining the parameters outline in Fig. 5, we can assess the circumstances under which quantum entanglement is generated. By implementing modifications to the



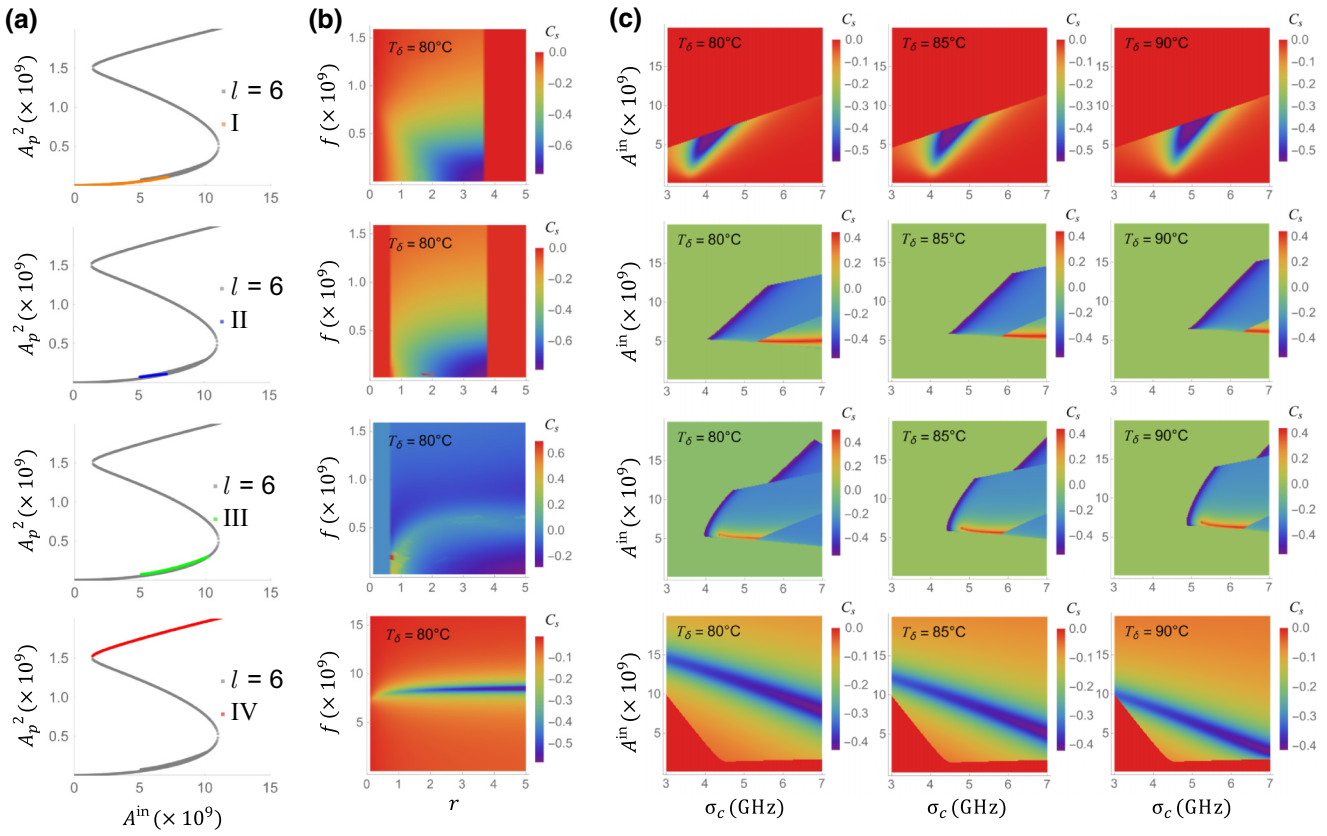


FIG. 9. (a) The four stages of the sixth mode. (b) The entanglement distribution in the regime of coupling rate r and observation frequency f ($\sigma_c = 4.5$ GHz, $A^{in} = 6 \times 10^9$). (c) The entanglement distribution in the regime of pump detuning σ_c and injected pump power A^{in} ($r = 1.222$, observation angular frequency $\omega = 10^4$ at stage I, II, and III, and $\omega = 6 \times 10^{10}$ at stage IV).

microresonator based on our design platform, we successfully generate bipartite entangled frequency combs with 12 channels (six pairs), as depicted in Fig. 6. It is assumed that $T_\delta = 80^\circ\text{C}$, $\sigma_c = 4.5$ GHz, and our QFC is under the influence of hysteresis [38].

Referring to Figs. 6(a) and 6(b), the S-type brown curve in Fig. 6(a) displays all the frequency modes below OPO threshold (spontaneous FWM process), whereas the colored bifurcation structure in Fig. 6(a) and the colored curves in Fig. 6(b) demonstrate all the frequency modes above OPO threshold (stimulated FWM process). Specifically, take $l = 4$ as an example. The solutions of Eq. (17) are depicted in Fig. 7. In stage I and stage IV, the orange curve and the red curve demonstrate that the comb-generation system is below OPO threshold. The signal-mode amplitude and the idler-mode amplitude are zero, while only intracavity pump-mode amplitude varies with injected pump amplitude. In stage II and stage III, the blue curve and the green curve represent that the comb-generation system is above OPO threshold. All the intracavity mode amplitudes fluctuate in response to the injected pump power. Although the remaining brown curve also represents the comb-generation system below

OPO threshold, according to Ref. [38], solutions in these ranges of unstable values do not apply to experimental situations.

The consequences of phase modulation above OPO threshold are apparent as the intracavity mode amplitude fluctuates in response to the injected pump power. This phenomenon can be attributed to the phase modulation that occurs when the pump power is increased to trigger the OPO. To compensate for the frequency shift introduced by phase modulation, it is necessary to pump the resonator with a detuning that exceeds the cavity linewidth. In addition, the detailed properties of the relationship between intracavity modes and injected pump mode is introduced in Ref. [34].

Then, we take the fourth and sixth mode ($l = 4$, $l = 6$) into consideration, which can be analyzed in four distinct stages, shown in Figs. 8(a) and Fig. 9(a). Stages I and IV denote a QFC that is below the threshold, and it is noteworthy that these two stages exhibit bistability, which means each stage converges to either stage depending on the detuning procedure employed. Correspondingly, stages II and III indicate a QFC that is above the threshold. By rotating different angles θ_+ and θ_- to locate the minimum

value of C_s , we can obtain a panoramic view of the QFC entanglement distribution. Figures 8(b) and 9(b) showcase the entanglement distribution in the coupling rate r and observation frequency f regime, assuming injected pump power $A^{\text{in}} = 6 \times 10^9$ and pump detuning $\sigma_c = 4.5$ GHz. We notice that the degree of entanglement increases as the coupling rate rises, while the strongest entanglement is not necessarily at $f=0$. In stage IV, the entanglement shape displays a double-peaked pattern, which is directly linked to the double maximum value of spectral noise density $S_a(\omega)$.

According to the silhouette in Figs. 8(b) and 9(b), we select the observation frequency point of $\omega = 10^4$ for stages I, II, and III, and $\omega = 6 \times 10^{10}$ for stage IV (under rotating-wave approximation). We set the coupling rate $r = 1.222$ to align with our microresonator design. Thus, we obtain the entanglement distribution in the regime of pump detuning σ_c and injected pump power A^{in} , shown in Figs. 8(c) and 9(c). We can roughly determine the range of injected pump power and pump detuning that can achieve relatively high entanglement. Once the injected pump power and pump detuning are determined, we can fine tune the cavity temperature to maximize its entanglement performance in the corresponding region, no matter our QFC is below threshold or above threshold.

V. CONCLUSION

In summary, we develop a platform for designing bipartite entangled quantum frequency combs based on silicon nitride microring resonators and employ bipartite entanglement criterion to quantify the influence of microresonator structure and cavity temperature on the degree of entanglement. With our quantum frequency comb, we are able to provide quantum entangled states in no fewer than 12 channels, making it a suitable solution for multichannel quantum information networks. Among these channels, we can optimize the entanglement degree of each mode at any stage under certain initially set injected pump power and pump detuning through temperature adjustment, which may give inspiration for better quantum resources and lead to better understanding of entanglement mechanism.

ACKNOWLEDGMENTS

This work is supported by the Key-Area Research and Development Program of Guangdong Province (Grant No. 2018B030325002), the National Natural Science Foundation of China (Grants No. 62075129, No. 61975119), the Open Project Program of SJTU-Pinghu Institute of Intelligent Optoelectronics (Grant No. 2022SPIOE204) and the Sichuan Provincial Key Laboratory of Microwave Photonics (Grant No. 2023-04).

- [1] M. Kues, C. Reimer, P. Roztocki, L. R. Cortés, S. Sciara, B. Wetzel, Y. Zhang, A. Cino, S. T. Chu, and B. E. Little, *et al.*, On-chip generation of high-dimensional entangled quantum states and their coherent control, *Nature* **546**, 622 (2017).
- [2] C. Reimer, M. Kues, P. Roztocki, B. Wetzel, F. Grazioso, B. E. Little, S. T. Chu, T. Johnston, Y. Bromberg, and L. Caspani, *et al.*, Generation of multiphoton entangled quantum states by means of integrated frequency combs, *Science* **351**, 1176 (2016).
- [3] C. Xiong, X. Zhang, A. Mahendra, J. He, D.-Y. Choi, C. Chae, D. Marpaung, A. Leinse, R. Heideman, and M. Hoekman, *et al.*, Compact and reconfigurable silicon nitride time-bin entanglement circuit, *Optica* **2**, 724 (2015).
- [4] F. Samara, A. Martin, C. Autelbert, M. Karlov, T. J. Kippenberg, H. Zbinden, and R. Thew, High-rate photon pairs and sequential time-bin entanglement with Si_3N_4 microring resonators, *Opt. Express* **27**, 19309 (2019).
- [5] Z. Yin, K. Sugiura, H. Takashima, R. Okamoto, F. Qiu, S. Yokoyama, and S. Takeuchi, Frequency correlated photon generation at telecom band using silicon nitride ring cavities, *Opt. Express* **29**, 4821 (2021).
- [6] V. D. Vaidya, B. Morrison, L. Helt, R. Shahrokshahi, D. Mahler, M. Collins, K. Tan, J. Lavoie, A. Repington, and M. Menotti, *et al.*, Broadband quadrature-squeezed vacuum and nonclassical photon number correlations from a nanophotonic device, *Sci. Adv.* **6**, eaba9186 (2020).
- [7] K. Wu, Q. Zhang, and A. W. Poon, Integrated Si_3N_4 microresonator-based quantum light sources with high brightness using a subtractive wafer-scale platform, *Opt. Express* **29**, 24750 (2021).
- [8] W. Wen, Z. Chen, L. Lu, W. Yan, W. Xue, P. Zhang, Y. Lu, S. Zhu, and X. S. Ma, Realizing an entanglement-based multiuser quantum network with integrated photonics, *Phys. Rev. Appl.* **18**, 024059 (2022).
- [9] Y. Zhang, M. Menotti, K. Tan, V. D. Vaidya, D. H. Mahler, L. G. Helt, L. Zatti, M. Liscidini, B. Morrison, and Z. Vernon, Squeezed light from a nanophotonic molecule, *Nat. Commun.* **12**, 2233 (2021).
- [10] M. A. Guidry, D. M. Lukin, K. Y. Yang, R. Trivedi, and J. Vučković, Quantum optics of soliton microcombs, *Nat. Photonics* **16**, 52 (2022).
- [11] C. Xiang, W. Jin, and J. E. Bowers, Silicon nitride passive and active photonic integrated circuits: Trends and prospects, *Photonics Res.* **10**, A82 (2022).
- [12] C. Xiang, J. Guo, W. Jin, L. Wu, J. Peters, W. Xie, L. Chang, B. Shen, H. Wang, and Q.-F. Yang, *et al.*, High-performance lasers for fully integrated silicon nitride photonics, *Nat. Commun.* **12**, 6650 (2021).
- [13] X. Xue, Y. Xuan, C. Wang, P.-H. Wang, Y. Liu, B. Niu, D. E. Leaird, M. Qi, and A. M. Weiner, Thermal tuning of Kerr frequency combs in silicon nitride microring resonators, *Opt. Express* **24**, 687 (2016).
- [14] C. Joshi, J. K. Jang, K. Luke, X. Ji, S. A. Miller, A. Klenner, Y. Okawachi, M. Lipson, and A. L. Gaeta, Thermally controlled comb generation and soliton modelocking in microresonators, *Opt. Lett.* **41**, 2565 (2016).
- [15] J. M. Dudley, G. Genty, and S. Coen, Supercontinuum generation in photonic crystal fiber, *Rev. Mod. Phys.* **78**, 1135 (2006).

- [16] I. Breunig, Three-wave mixing in whispering gallery resonators, *Laser. Photonics Rev.* **4**, 569 (2016).
- [17] V. Brasch, M. Geiselmann, T. Herr, G. Lihachev, M. H. Pfeiffer, M. L. Gorodetsky, and T. J. Kippenberg, Photonic chip-based optical frequency comb using soliton Cherenkov radiation, *Science* **351**, 357 (2016).
- [18] C. Godey, I. V. Balakireva, A. Coillet, and Y. K. Chembo, Stability analysis of the spatiotemporal Lugiato-Lefever model for Kerr optical frequency combs in the anomalous and normal dispersion regimes, *Phys. Rev. A* **89**, 063814 (2014).
- [19] A. Arbabi and L. L. Goddard, Measurements of the refractive indices and thermo-optic coefficients of Si_3N_4 and SiO_x using microring resonances, *Opt. Lett.* **38**, 3878 (2013).
- [20] G. Huang, E. Lucas, J. Liu, A. S. Raja, G. Lihachev, M. L. Gorodetsky, N. J. Engelsen, and T. J. Kippenberg, Thermorefractive noise in silicon-nitride microresonators, *Phys. Rev. A* **99**, 061801(R) (2019).
- [21] Z. Vernon and J. E. Sipe, Spontaneous four-wave mixing in lossy microring resonators, *Phys. Rev. A* **91**, 053802 (2015).
- [22] Z. Vernon and J. E. Sipe, Strongly driven nonlinear quantum optics in microring resonators, *Phys. Rev. A* **92**, 033840 (2015).
- [23] T. Debuisschert, A. Sizmann, E. Giacobino, and C. Fabre, Type-II continuous-wave optical parametric oscillators: Oscillation and frequency-tuning characteristics, *JOSA B* **10**, 1668 (1993).
- [24] P. Rabiei, W. H. Steier, C. Zhang, and L. R. Dalton, Polymer micro-ring filters and modulators, *J. Lightwave Technol.* **20**, 1968 (2002).
- [25] Y. Xuan, Y. Liu, L. T. Varghese, A. J. Metcalf, X. Xue, P.-H. Wang, K. Han, J. A. Jaramillo-Villegas, A. Al Noman, and C. Wang, *et al.*, High-Q silicon nitride microresonators exhibiting low-power frequency comb initiation, *Optica* **3**, 1171 (2016).
- [26] T. C. Briles, S.-P. Yu, T. E. Drake, J. R. Stone, and S. B. Papp, Generating octave-bandwidth soliton frequency combs with compact low-power semiconductor lasers, *Phys. Rev. Appl.* **14**, 014006 (2020).
- [27] D. J. Wilson, K. Schneider, S. Hönl, M. Anderson, Y. Baumgartner, L. Czornomaz, T. J. Kippenberg, and P. Seidler, Integrated gallium phosphide nonlinear photonicics, *Nat. Photonics* **14**, 57 (2020).
- [28] X. Xue, Y. Xuan, Y. Liu, P.-H. Wang, S. Chen, J. Wang, D. E. Leaird, M. Qi, and A. M. Weiner, Mode-locked dark pulse Kerr combs in normal-dispersion microresonators, *Nat. Photonics* **9**, 594 (2015).
- [29] K. Luke, Y. Okawachi, M. R. Lamont, A. L. Gaeta, and M. Lipson, Broadband mid-infrared frequency comb generation in a Si_3N_4 microresonator, *Opt. Lett.* **40**, 4823 (2015).
- [30] Y. K. Chembo, Quantum dynamics of Kerr optical frequency combs below and above threshold: Spontaneous four-wave mixing, entanglement, and squeezed states of light, *Phys. Rev. A* **93**, 033820 (2016).
- [31] Y. Wang, K. D. Jöns, and Z. Sun, Integrated photon-pair sources with nonlinear optics, *Appl. Phys. Rev.* **8**, 011314 (2021).
- [32] M. Gao, Q.-F. Yang, Q.-X. Ji, H. Wang, L. Wu, B. Shen, J. Liu, G. Huang, L. Chang, and W. Xie, *et al.*, Probing material absorption and optical nonlinearity of integrated photonic materials, *Nat. Commun.* **13**, 3323 (2022).
- [33] S. J. Whalen and H. J. Carmichael, Time-local Heisenberg-Langevin equations and the driven qubit, *Phys. Rev. A* **93**, 063820 (2016).
- [34] A. B. Matsko, A. A. Savchenkov, D. Strekalov, V. S. Ilchenko, and L. Maleki, Optical hyperparametric oscillations in a whispering-gallery-mode resonator: Threshold and phase diffusion, *Phys. Rev. A* **71**, 033804 (2005).
- [35] L.-M. Duan, G. Giedke, J. I. Cirac, and P. Zoller, Inseparability criterion for continuous variable systems, *Phys. Rev. Lett.* **84**, 2722 (2000).
- [36] G. Ferrini, I. Fsaifes, T. Labidi, F. Goldfarb, N. Treps, and F. Bretenaker, Symplectic approach to the amplification process in a nonlinear fiber: Role of signal-idler correlations and application to loss management, *JOSA B* **31**, 1627 (2014).
- [37] V. Giovannetti, S. Mancini, D. Vitali, and P. Tombesi, Characterizing the entanglement of bipartite quantum systems, *Phys. Rev. A* **67**, 022320 (2003).
- [38] Y. K. Chembo and N. Yu, Modal expansion approach to optical-frequency-comb generation with monolithic whispering-gallery-mode resonators, *Phys. Rev. A* **82**, 033801 (2010).